Diffusion of Flexible Random-Coil Dextran Polymers Measured in Anisotropic Brain Extracellular Space by Integrative Optical Imaging

Fanrong Xiao,* Charles Nicholson,† Jan Hrabe,‡* and Sabina Hrabětová*†

*Department of Anatomy and Cell Biology, The Robert F. Furchgott Center for Neural and Behavioral Science, State University of New York, Downstate Medical Center, Brooklyn, New York; †Department of Physiology and Neuroscience, New York University School of Medicine, New York, New York; and ‡Center for Advanced Brain Imaging, Nathan S. Kline Institute for Psychiatric Research, Orangeburg, New York

ABSTRACT There are a limited number of methods available to quantify the extracellular diffusion of macromolecules in an anisotropic brain region, e.g., an area containing numerous aligned fibers where diffusion is faster along the fibers than across. We applied the integrative optical imaging method to measure diffusion of the fluorophore Alexa Fluor 488 (molecular weight (MW) 547) and fluorophore-labeled flexible random-coil dextran polymers (dex3, MW 3000; dex75, MW 75,000; dex282, MW 282,000; dex525, MW 525,000) in the extracellular space (ECS) of the anisotropic molecular layer of the isolated turtle cerebellum. For all molecules, two-dimensional images acquired an elliptical shape with major and minor axes oriented along and across, respectively, the unmyelinated parallel fibers. The effective diffusion coefficients, D^*_{major} and D^*_{minor}, decreased with molecular size. The diffusion anisotropy ratio ($DAR = D^*_{major}/D^*_{minor}$) increased for Alexa Fluor 488 through dex75 but then unexpectedly reached a plateau. We argue that dex282 and dex525 approach the ECS width and deform to diffuse. In support of this concept, scaling theory shows the diffusion behavior of dex282 and dex525 to be consistent with transition to a reptation regime, and estimates the average ECS width at ~31 nm. These findings have implications for the interstitial transport of molecules and drugs, and for modeling neurotransmitter diffusion during ectopic release and spillover.

INTRODUCTION

In brain regions containing numerous aligned fibers, extracellular diffusion is anisotropic, i.e., faster along the fibers than across them (1–4), implying a preferential pathway for the transport of molecules in the extracellular space (ECS) (1,5). To date, ECS anisotropy has been measured using diffusion-based techniques employing a small cation (tetramethylammonium (TMA) molecular weight (MW) 74 (1–3)) or a macromolecule of a single molecular size (fluorophore-labeled dextran, MW 70,000 (4)). However, the ECS accommodates the diffusion of a large range of endogenous macromolecules, and it is an exclusive route for the interstitial transport of polymer-based drug carriers, therapeutic proteins, and virus-enclosed genes (6,7). Here, we extended the integrative optical imaging (IOI) method developed for isotropic media (8,9) to quantify diffusion of a small fluorophore and a series of fluorophore-labeled polymers in the anisotropic molecular layer (ML) of the isolated turtle cerebellum.

Anisotropic diffusion in the brain frequently has been detected using the magnetic resonance technique known as diffusion tensor imaging (DTI; (10,11)) and the real-time iontophoretic method (RTI) employing TMA (1–3). The DTI studies showed that the diffusion anisotropy ratio ($DAR = ADC_{major}/ADC_{minor}$, where ADC_{major} and ADC_{minor} are the apparent diffusion coefficients of water along and across the fibers, respectively) ranged from 2 to 4 for a variety of fiber types and animal species (for a review, see (12)). Because DTI combines signals coming from intra- and extracellular compartments, these studies do not reliably measure anisotropy in either of these domains. Unlike DTI, the RTI method (13) measures diffusion exclusively in the ECS. The probe molecule, most commonly TMA, is released into the ECS from an iontophoretic microelectrode and detected by an ion-selective microelectrode positioned nearby. Because microelectrodes can be repositioned or increased in number, the method is well suited to determine the diffusion along the principal axes of the diffusion tensor (1). A limitation of the RTI method is that it only works with a limited number of small charged molecules, namely those for which an ion-selective microelectrode can be made (13), and the method does not measure the diffusion of large or uncharged molecules.

Clearly, there is a need for a technique that can measure the diffusion of macromolecules in anisotropic brain regions. For this purpose, we adopted the IOI method (8,9). The IOI theory was extended to an anisotropic medium and two different approaches to estimate the *DAR* were implemented. Experiments were performed in the ML of the isolated turtle cerebellum, an anisotropic brain region rich in unmyelinated parallel fibers (1). We first demonstrated the utility of this new IOI application with a small fluorophore, Alexa Fluor 488 (AF, MW 547), where the influence of molecular size on the experimental results is minimal (14). The diffusion measurements were then repeated with a range of fluorophore-labeled flexible random-coil dextran polymers (i.e., dex3, MW 3000; dex75, 75,000; dex282, 282,000; dex525, 525,000).

Submitted October 29, 2007, and accepted for publication April 7, 2008.

Address reprint requests to Dr. Sabina Hrabětová, Tel.: 718-221-5392; E-mail: sabina.hrabetova@downstate.edu.

Editor: David W. Piston.

0006-3495/08/08/1382/11 $2.00

doi: 10.1529/biophysj.107.124743

MATERIALS AND METHODS

Preparation of isolated turtle cerebellum

The experiments were conducted at New York University School of Medicine in accordance with National Institutes of Health guidelines and local Institutional Animal Care and Use Committee regulations.

The cerebellum was isolated from adult North American pond turtles (*Trachemys scripta elegans*, 450–550 g) of either sex, as described previously (1). A total of 14 animals were used in this study; and each molecule was measured in cerebella from three or more turtles. The animals were anesthetized with ketamine (40 mg/kg, i.m.) and decapitated using a guillotine. The cranium was opened, and the brain removed into artificial cerebrospinal fluid (ACSF) containing (in mmol/L): NaCl 103, KCl 5, $NaHCO_3$ 40, $MgCl_2$ 5, $CaCl_2$ 2, D-glucose 20. The ACSF was gassed with 95% O_2 and 5% CO_2 mixture to buffer pH at 7.6. The osmolality of ACSF, determined with a freezing point-depression osmometer (Osmette A No. 5002; Precision Systems, Natick, MA), was 295–305 mosmol/kg. The cerebellum was dissected free from the brainstem under a stereomicroscope and the pia mater was removed from the dorsal surface with fine forceps.

The turtle cerebellum is shaped like a disk ~5-mm wide and 800-μm thick (15). Molecular and granular layers, each occupying approximately half the thickness, lie above and below the narrow Purkinje cell layer. A schematic with a typical recording site in the ML is shown in Fig. 1 *a*.

For diffusion measurements, the cerebellum was placed in a submersion recording chamber (model RC-27L; Warner Instruments, Hamden, CT) with its dorsal surface facing up, and was superfused with ACSF at a flow rate of 2.0 mL/min. The temperature was monitored using a temperature controller (model TC-344B; Warner Instruments).

Integrative optical imaging (IOI) method

In the IOI method, fluorophore-labeled molecules are pressure-injected from a glass micropipette into brain tissue or dilute agarose gel (approximating a free medium) and a sequence of images is captured with a charge-coupled device (CCD) camera attached to a compound microscope equipped for epifluorescence. The image sequence is analyzed to extract the effective diffusion coefficient (D^*, $cm^2\ s^{-1}$) and the free diffusion coefficient (D, $cm^2\ s^{-1}$) in brain tissue and agarose gel, respectively. The extracellular tortuosity, a measure of tissue hindrance imposed on the diffusion by the extracellular microenvironment of the brain, is calculated as $\lambda = (D/D^*)^{1/2}$ (13,16).

This study measured diffusion of a small fluorophore, AF (cat. No. A10436, Invitrogen, Carlsbad, CA) and a series of dextran polymers (dex3 labeled with Texas Red, cat. No. D-3329, from Invitrogen, and several FITC-labeled dextrans: dex75, cat. No. FD-70S; dex282, cat. No. FD-250S; and dex525, cat. No. FD-500S, from Sigma-Aldrich, St. Louis, MO). Each fluorescent molecule was dissolved in a solution of 150 mM NaCl to a final concentration of 1 mM for AF and dex3, 0.1 mM for dex75, and 0.01 mM for dex282 and dex525. The solution of fluorescent molecules was released from a glass micropipette (pulled from thin-wall glass tubing, cat. No. 6170, A-M System, Carlsborg, WA) by a brief pulse of compressed nitrogen (10–200 ms, 10–20 psi) controlled by an electronic valve (Parker Hannifin, Fairfield, NJ). The micropipette, held in a robotic micromanipulator (MP 285, Sutter Instrument, Novato, CA), was advanced into the specimen at an angle of 31° from the horizontal plane. The tip (diameter 2–4 μm) was positioned 200 μm below the dorsal surface of cerebellum or 1000 μm below the surface in dilute agarose gel (0.3% in 150 mM NaCl, NuSieve GTG Agarose, FMC BioProducts, Rockland, ME). The injection volumes using the described delivery paradigm are <1 nL (8,14,17).

The excitation light from a 75 W xenon source mounted on the epifluorescent port of a model No. BX61WI compound microscope (Olympus America, Melville, NY) was directed to the tissue using a dichroic mirror with either Texas Red or fluorescein filter sets. A time sequence of images of the diffusing fluorescent molecules (Fig. 1 *b*) was recorded with a cooled CCD camera (model No. CH350, Photometrics, Tucson, AZ) attached to the

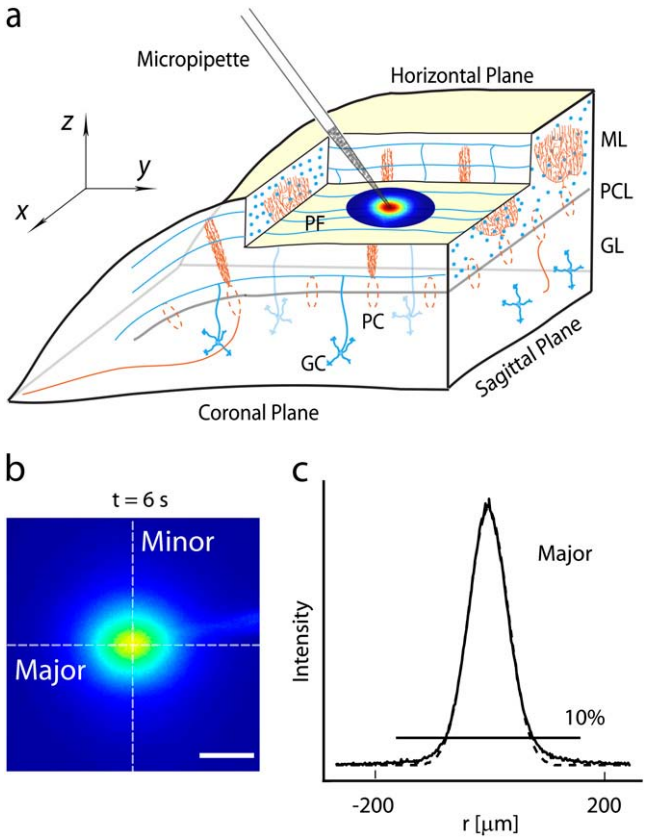

FIGURE 1 Anisotropic extracellular diffusion measured with the IOI method. (*a*) Schematic of turtle cerebellum (*ML*, molecular layer; *PCL*, Purkinje cell layer; *GL*, granular layer; *PF*, parallel fiber; *PC*, Purkinje cell; and *GC*, granular cell). Diffusion measurements were done in the horizontal plane (*x*,*y*) of the ML. (*b*) A time sequence of two-dimensional images (scale bar 100 μm) of three-dimensional diffusion cloud was captured by the charge-coupled device (CCD) camera; panel shows a single image at $t = 6$ s. Dashed lines show the major and the minor axes of elliptical diffusion cloud. (*c*) The intensity profiles along major (*solid line*) and minor (not shown) axes were extracted and fitted with an appropriate theoretical model (*dashed line*). The lower 10% of the curves were not used in the fitting.

microscope. The sequence acquisition intervals and duration depended on the molecular weight of the molecule and the diffusion medium; e.g., in the ML, 20 images were captured over 50 s for AF while 60 images were taken over 20 min for dex525. For sequence acquisition durations longer than 60 s (i.e., dex75, dex282, and dex525 in the ML), a shutter in the excitation light path (model Uniblitz VS35 with T132 controller, Vincent Associates, Rochester, NY) was closed after each exposure to prevent photobleaching. The images were acquired using V++ software (Digital Optics, Auckland, New Zealand) and analyzed with a MATLAB-based (The MathWorks, Natick, MA) program developed in-house (14).

Diffusion measurements made in the agarose gel were processed using a two-step data analysis (8,18). After subtracting the background image acquired before the injection, the intensity profiles were extracted along row, column, and two diagonal directions from each image and fitted with a Gaussian curve to obtain the values of $\gamma^2/4$ (see Theory). The value of D was obtained by applying a linear regression to the time series of $\gamma^2/4$. The analysis of data obtained in the anisotropic ML will be described in Theory.

Diffusion coefficients, D and D^*, were measured at room temperature (22–28°C) and corrected to 25°C using the Stokes-Einstein relation $D_{25} = D\,(T_{25}/T)\,(\eta/\eta_{25})$, where T is the absolute temperature and η is the viscosity of water (19).

THEORY

In an anisotropic medium with principal effective diffusion coefficients D_x^*, D_y^*, and D_z^* in directions of the x, y, and z axes, the concentration at time t and position (x, y, z), resulting from a point source of strength Q placed at the origin at time $t = 0$, is given (8,20) as

$$C(x,y,z,t) = \frac{Q}{\pi^{3/2}\gamma_x\gamma_y\gamma_z}\exp\left[-\left(\frac{x^2}{\gamma_x^2}+\frac{y^2}{\gamma_y^2}+\frac{z^2}{\gamma_z^2}\right)\right], \quad (1)$$

where

$$\gamma_i^2 = 4D_i^* t \quad \text{for} \quad i = x, y, z. \quad (2)$$

When the source is a micropipette that releases a volume U at concentration C_f into a medium with volume fraction α, then $Q = U\,C_f/\alpha$ (8).

For an ideal point source, a similar approximation to that used previously (8,9) can be applied to deduce the two-dimensional projection of a three-dimensional diffusion cloud. Providing the axis of the optical system coincides with the principal diffusion axis z, the image intensity expressed in object space coordinates is

$$I(x,y,t) = E(t)\exp\left[-\left(\frac{x^2}{\gamma_x^2}+\frac{y^2}{\gamma_y^2}\right)\right]. \quad (3)$$

The values of γ_x and γ_y from the three-dimensional Eq. 1 are therefore preserved in the projected image. The defocusing influence of the microscope objective's point-spread function is included in the amplitude scaling term $E(t)$. However, the dependency on the x and y coordinates is contained in the two-dimensional Gaussian exponential term, and is thus governed only by the two factors γ_x and γ_y. This makes the analysis relatively simple.

The diffusion anisotropy ratio is given by $DAR = D_x^*/D_y^*$, where we can assume $D_x^* > D_y^*$. The shape of a projected diffusion cloud at any given time can be characterized by the radii R_x and R_y, defined as full width at half-maximum of the image profiles along the x and y axes, respectively. For an ideal point injection, each radius is directly proportional to the corresponding γ_i and the ratio R_x/R_y, and therefore has a simple relation with the DAR (21):

$$DAR = \left(\frac{R_x}{R_y}\right)^2. \quad (4)$$

In an experiment using pressure injection, a finite volume source rather than a point source is typically obtained. The finite injection volume may either infiltrate the ECS or form a cavity (22). Because the injection volume is <1 nL in a typical IOI experiment, it is reasonable to approximate this source by an ideal point source preceding the actual injection by a time interval t_{0i} (18). The image intensity has the same expression as in Eq. 3 except that Eq. 2 is replaced by

$$\gamma_i^2 = 4D_i^*(t + t_{0i}). \quad (5)$$

The relation between R_x/R_y and the DAR for a volume source can be deduced from Eqs. 3 and 5,

$$DAR = \left(\frac{R_x}{R_y}\right)^2\left(\frac{t+t_{0y}}{t+t_{0x}}\right), \quad (6)$$

where t_{0x} and t_{0y} are the time shifts of the virtual point sources associated with measurements along the x and the y axes, respectively. If $t_{0x} = t_{0y}$, Eq. 6 can be simplified to Eq. 4. For $t_{0x} \neq t_{0y}$, the DAR approaches $(R_x/R_y)^2$ when

$$t \gg |t_{0x} - t_{0y}|. \quad (7)$$

Equations 5 and 6 suggest two different approaches to quantify the DAR: either first estimate D_x^* and D_y^* and then calculate the DAR (D^* method), or estimate the DAR directly from R_x and R_y without obtaining the effective diffusion coefficients (radii ratio method).

The D^* method extends the original technique for extracting D^* in an isotropic medium. It has four steps.

First, the major and minor axes are extracted from each image. Briefly, the maximum and minimum values in a given image, I_{max}, and I_{min}, respectively, are determined and two parameters defined, $\Delta = \varepsilon\,(I_{max} - I_{min})$ and $I_{mean} = (I_{min} + I_{max})/2$. The exact value of ε is not critical as long as it is small ($\varepsilon \ll 1$), typically $\varepsilon = 0.005$. *A* set of coordinates (x,y) satisfying condition $I_{mean} - \Delta \leq I(x, y) \leq I_{mean} + \Delta$ is then found, forming a band through the image at the half-height of the Gaussian surface with a tolerance in the image intensity given by $\pm\Delta$. A slightly modified version of the robust ellipse fitting algorithm described by Fitzgibbon et al. (23) is applied to determine the center of the ellipse, the major and minor axes, and their orientations with respect to the image frame (Fig. 1 *b*).

Second, the intensity profiles along the major and minor axes are extracted for each image and fitted with Gaussian curves (Fig. 1 *c*) to calculate the values of $\gamma_i^2/4$. The lower 10% of the experimental curves are excluded because of possible distortion by light scattering in the tissue (Fig. 1 *c*; (8)).

Third, D_{major}^* (i.e., D_x^*) and D_{minor}^* (i.e., D_y^*) are estimated by fitting $\gamma_i^2/4$ as functions of time using a linear regression.

Fourth, the DAR is calculated as D_{major}^*/D_{minor}^*.

The radii ratio method estimates the DAR directly from the shape of a two-dimensional projection of the diffusion cloud. Initially, the ellipse with the major and the minor axes is determined from each image, as described above for the D^* method. The ratio R_{major}/R_{minor} (i.e., R_x/R_y) is then calculated and the DAR is estimated. For an ideal point source, the DAR can be obtained using R_{major} and R_{minor} from any image taken after the injection (Eq. 4). However, for a finite volume injection, the DAR depends not only on R_{major} and R_{minor} but also on t_{0x} and t_{0y} (Eq. 6). It is therefore necessary to record for a sufficiently long time period, making the difference between t_{0x} and t_{0y} negligible. After the radii ratio stabilizes

for times $t > t_{threshold}$, Eq. 4 becomes a good approximation for Eq. 6.

Numerical simulations

Numerical simulations were employed to assess the limitations of the radii ratio method and compare it with the D^* method. In particular, we tested how the time $t_{threshold}$ depends on the magnitude of D^* and on the size and shape of the finite injection volume. A series of images resulting from elliptical injections of point particles into an anisotropic medium characterized by D^*_{major} and D^*_{minor} were simulated with a program written in MATLAB. The simulated data sets were processed by both methods.

To examine the effect of D^* magnitude, the values of *DAR* were estimated with the radii ratio method for two sets of D^* values (first set was $D^*_{major} = 2.12 \times 10^{-6}$ cm^2 s^{-1} and $D^*_{minor} = 1.44 \times 10^{-6}$ cm^2 s^{-1}, mimicking the experimental values obtained with AF; in the second set, both D^*_{major} and D^*_{minor} were 10 times smaller than in the first set). The injection was spherical with the diameter $d = 100$ μm. Fig. 2 *a* shows that the *DAR* estimates stabilized much faster for larger D^* values. In contrast, the *DAR* was still increasing at 200 s for the second set of smaller D^* values. This is easily explained because for any given injection diameter, the times t_{0x} and t_{0y} become larger for slower molecules ($t_{0i} \propto 1/D^*_i$). However, all time variables are scaled by the diffusion coefficients in the same way, and the effect of slower molecules on t_{0i} can be reversed by simply extending the recording period t. Unlike the radii ratio method, the D^* method utilizes the whole image time series and provides correct answers for any t_{0x} and t_{0y} even when the condition given by Eq. 7 is not satisfied.

The effect of injection size was examined using three spherical injection diameters (2 μm, 100 μm, and 200 μm) while keeping the same anisotropic environment ($D^*_{major} = 2.12 \times 10^{-6}$ cm^2 s^{-1} and $D^*_{minor} = 1.44 \times 10^{-6}$ cm^2 s^{-1}, giving theoretical $DAR = 1.47$). The smallest injection diameter approximates a point source. An experimentally realistic diameter of 100 μm corresponds to a volume of 0.1 nL (8,14,17) injected into ECS occupying 30% of the tissue volume. This ECS volume fraction matches the experimental value obtained in the ML of an isolated turtle cerebellum (1). The largest diameter ($d = 200$ μm) represents an extreme case of a very large injection, not typically used in the experiments. Fig. 2 *b* demonstrates that for a point source, the *DAR* stabilizes instantaneously (estimated $DAR = 1.49$). As expected, the stabilization takes longer for larger injection diameters (Fig. 2 *b*) because the time offsets t_{0i} are proportional to the injection diameters ($t_{0i} \propto d_i^2$). As before, the D^* method is unaffected.

The projection of the initial injection volume encountered in the experiments often resembles an ellipse rather than a circle. To evaluate the effect of this asymmetry on the *DAR* estimates, the same anisotropic environment as before was simulated ($D^*_{major} = 2.12 \times 10^{-6}$ cm^2 s^{-1} and $D^*_{minor} = 1.44 \times 10^{-6}$ cm^2 s^{-1}) but the injection volumes were elliptical with varying degrees of eccentricity. For all injections, the diameter d_{major} was set to 100 μm while d_{minor} was 200, 100, 82, and 50 μm. At time $t = 0$, $(R_{major}/R_{minor})^2 = (d_{major}/d_{minor})^2$ was 0.25, 1.00, 1.49, and 4.00 while the theoretical *DAR* was always 1.47. As documented in Fig. 3, the *DAR* estimates provided by the radii ratio method were increasing or decreasing with time from their initial values to ultimately converge to 1.49 for all injections. Note that for $d_{major}/d_{minor} = 0.5$, the major axis flips (marked by an *arrowhead* in Fig. 3) to align with the direction of D^*_{major}. The inset of Fig. 3 documents that estimates obtained by the D^* method do not depend on the eccentricity in the initial ellipse at all. These estimates were very close to the correct theoretical value for all injection shapes considered. The initial diameter d_{minor} merely affected the time offset t_{0y}, which was reflected in the vertical offsets of the fitted lines.

In summary, the simulations suggest that the D^* method is much more robust than the radii ratio method. The radii ratio method is more sensitive to the size of the injection volume, as well as to its shape. The radii-ratio method is very simple, however, and can be successfully employed for small injection volumes. When it fails, this is easily detected by observing the time course of the generated *DAR* estimates.

RESULTS

Although the *DAR*s obtained by the IOI method involve only the two principal diffusion coefficients in a horizontal plane, it is useful to note that the IOI method itself assumes three-

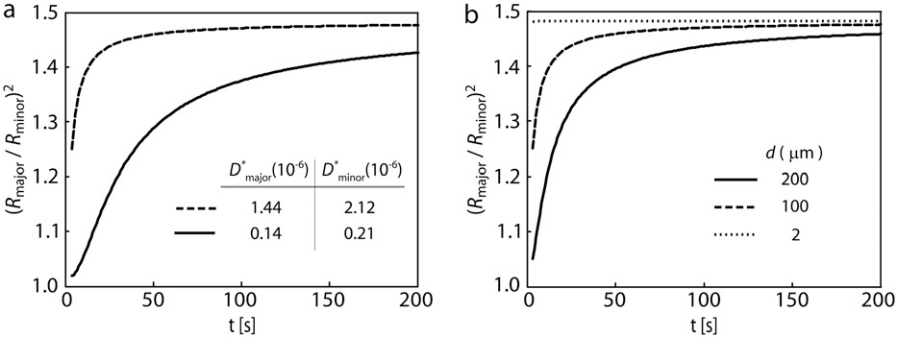

FIGURE 2 Estimation of the *DAR* from simulations: radii ratio method. (*a*) Injection volume diameter d was set at 100 μm (spherical injection volume 0.1 nL with volume fraction 0.30). Two sets of D^*_{major} and D^*_{minor} were used. The radii ratio stabilizes faster for the larger D^*. (*b*) The values of D^*_{major} and D^*_{minor} were set at 2.12×10^{-6} cm^2 s^{-1} and 1.44×10^{-6} cm^2 s^{-1}, respectively. Three different spherical injection volumes, with diameters $d = 2$, 100, 200 μm, were used. The radii ratio stabilizes faster for a small injection.

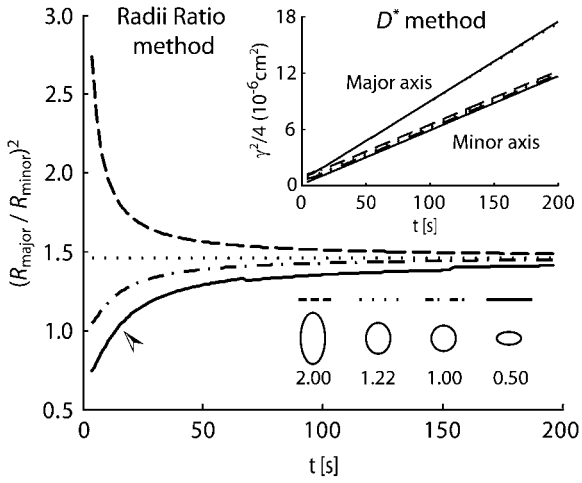

FIGURE 3 Estimation of the *DAR* from simulations: radii ratio method versus D^* method. Several elliptical injections with R_{major}/R_{minor} equal to 2.00, 1.22, 1.00, and 0.5 at $t = 0$ s were simulated and analyzed. It took >150 s to obtain the value of *DAR* with radii ratio method. By contrast, the D^* method (*inset*) can quantify the *DAR* at any time point after the injection from as few as two subsequent images (in practice, the whole series is analyzed). See text for details.

dimensional diffusion. The defocused point-spread function of the microscope objective then results in a weighted integration of the light intensity that is largely limited to a thin horizontal slab through the three-dimensional cloud of diffusing molecules and centered on the plane of focus (typically located at 200-μm depth in brain tissue). The effective thickness of this slab is a function of the depth of field, ~14 μm with our setup (9). As long as one principal axis of the diffusion tensor coincides with the optical axis of the objective, the diffusion along this axis does not influence the anisotropy results in the two remaining horizontal directions (see Theory). However, this also means that no information can be obtained about the diffusion in the vertical axis.

Free diffusion coefficient of AF and dextran polymers

We first measured D for AF, dex3, dex75, dex282, and dex525 in dilute agarose gel (0.3% agarose in 150 mM NaCl). Values of D are used later to estimate the hydrodynamic diameter (d_H) and diameter of gyration (d_G) of molecules in a solution, and to calculate λ. In Fig. 4 *a*, a sequence of representative images of AF is shown. This data set was also analyzed with the program developed for the anisotropic diffusion. The *DAR* estimates were smaller than 1.1 for all images (Fig. 4 *e*). The linear regression curves fitted to the time series of $\gamma^2/4$ extracted along major and minor axes almost overlap (Fig. 4 *f*), indicating isotropic diffusion ($DAR = 1.04$; $D_{major} = 4.33 \times 10^{-6}$ cm^2 s^{-1}; $D_{minor} = 4.14 \times 10^{-6}$ cm^2 s^{-1} at 25°C). As expected, diffusion of dextran polymers in agarose gel was also isotropic (data not shown). The values of D are summarized in Table 1.

Anisotropic diffusion of AF in the ML

We next measured diffusion of AF in the horizontal plane (x,y) in the ML (Fig. 1 *a*). Compared to agarose gel, the diffusion cloud of AF in the ML acquired an elliptical shape and dispersed more slowly (Fig. 4 *b*). As AF diffused in the ML, the *DAR* estimates increased from ≈1 (spherical injection) to 1.48 within 20 s, and remained stable thereafter (Fig. 4 *e*). The *DAR* obtained with the radii ratio method was thus 1.48. The experimental *DAR* estimate versus time curve (Fig. 4 *e*) fell between the simulated curves with d equal to 2 and 100 μm (Fig. 2 *b*), indicating an injection volume smaller than 0.1 nL (assuming penetration into an ECS with a volume fraction of 0.3). This injection volume agrees with previous estimates (8,14,17).

Use of the D^* method to evaluate data is documented in Fig. 4, *c*, *d*, and *f*. Representative examples of data superimposed on the theoretical curves are shown in Fig. 4 *c*, and a series of theoretical curves for both axes is shown in Fig. 4 *d*. At $t = 0$ s, the theoretical curves overlap. Over time, the peaks of both curves corresponding to the injection site stay overlapped but the major axis (*blue curve*) expands faster than the minor axis (*red curve*), resulting in a higher extracellular concentration of the fluorophore along the parallel fibers. The D^*_{major} and D^*_{minor} values ($D^*_{major} > D^*_{minor}$, $p < 0.001$, Wilcoxon Signed Rank Test) were obtained from curves of $\gamma^2/4$ versus time (Fig. 4 *f*), and λ_{major}, λ_{minor} and *DAR* were calculated. The *DAR* was 1.48, which agrees well with the result obtained by the radii ratio method. The D^*, λ, and *DAR* obtained in all experiments are given in Table 1.

Although the injection shown in Fig. 4 *b* was spherical, ~80% of the injections produced a cloud that initially had an elongated shape. Seventy percent of the injections started with radii ratio smaller than the square root of *DAR* obtained by the D^* method while 10% of the injections had a larger initial radii ratio. As shown by the simulations (Fig. 3), the elongated shape may prolong the time necessary to reach the $t_{threshold}$ in the radii ratio method but it has negligible effect on the D^* method.

In summary, the AF was successfully employed to show the utility of the IOI method in quantifying anisotropic diffusion in the ECS. The two methods of estimating the *DAR* arrived at similar values, thus demonstrating the applicability of both approaches for small molecules.

Anisotropic diffusion of dextran polymers in the ML

We next repeated the diffusion measurements in the ML for dex3, dex75, dex282, and dex525. For all dextran polymers, the diffusion cloud acquired an elliptical shape. The molecules diffused more slowly and the hindrance imposed by the tissue (λ) increased with molecular size. The representative data sets for dex75 and dex525 are shown in Fig. 5. The D^* ($D^*_{major} > D^*_{minor}$, $p < 0.001$, t-test), λ, and the *DAR* values obtained in all experiments are summarized in Table 1. We

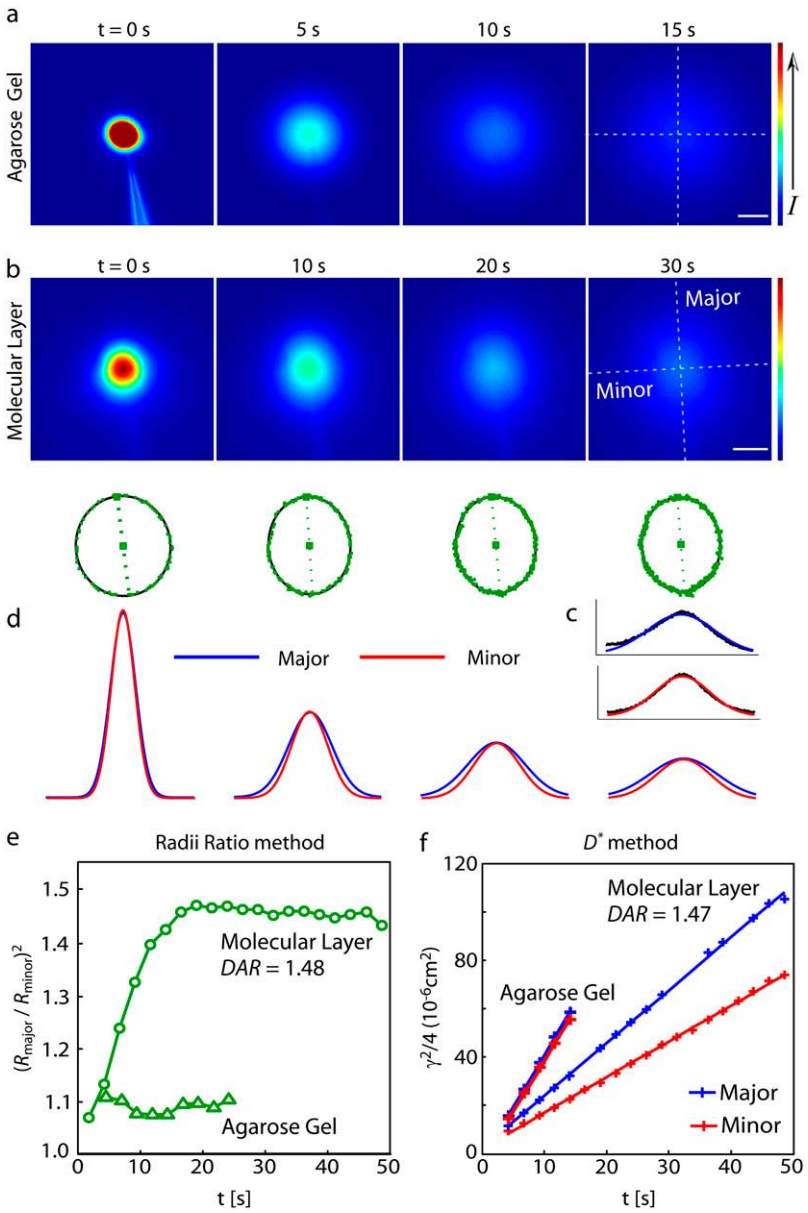

FIGURE 4 Diffusion of AF in agarose gel and ML of isolated turtle cerebellum. (*a*) Sequence of images taken after the injection of AF in agarose gel (scale bar 100 μm). The first image taken shortly after the injection is labeled as $t = 0$ s here and elsewhere. (*b*) Sequence of images taken in the ML (scale bar 100 μm). Extracted elliptical contours are shown below the images. (*c*) Fluorescence intensity profiles (*black*) extracted at $t = 30$ s along major and minor axes are superimposed with theoretical curves (*blue*, major; *red*, minor). (*d*) Theoretical curves obtained along major and minor axes at times as in panel *b* are shown superimposed to emphasize the differences in the shape between major and minor axes. (*e*) After a spherical injection, the *DAR* estimate gradually increased and stabilized at $\sim$ 20 s in anisotropic ML (*circles*). In isotropic dilute agarose gel, the *DAR* estimate remained <1.1 (*triangles*). (*f*) The values of D^*_{major} and D^*_{minor} were estimated from the $\gamma^2/4$ versus time curves. In anisotropic ML, the values of D^*_{major} and D^*_{minor} were 24.5×10^{-7} cm^2 s^{-1} and 16.7×10^{-7} cm^2 s^{-1}, respectively, at 25°C. In isotropic dilute agarose gel, the values of D^*_{major} (43.3×10^{-7} cm^2 s^{-1}) and D^*_{minor} (41.4×10^{-7} cm^2 s^{-1}) obtained at 25°C were similar as indicated by overlapping $\gamma^2/4$ versus time curves (*crosses*, data; *lines*, linear regression).

note that the $\gamma^2/4$ versus curves for dex282 and dex525 were not always linear at early times (Fig. 5 *c*); these time intervals (i.e., initial 100 s and 200 s for dex282 and dex525, respectively) were excluded from the analysis.

For dextran polymers, the *DAR* (Table 1) was quantified with the D^* method because the radii ratio method would require very long recording times. In fact, when we made a comparison with dex75 and AF using the ratio-radii method we found that AF stabilized at $\sim$20 s, while the *DAR* estimates for dex75 kept increasing beyond 200 s. This confirmed that, unless longer records are obtained, the radii ratio method is not suitable for large molecules.

In summary, the diffusion of dextran polymers was anisotropic in the ML and λ increased with molecular size, indicating growing hindrance as molecules increase in size.

DAR depends on the size of diffusing molecules

One important outcome of this study is the quantification of the *DAR* for a series of molecules spanning a large range of sizes (Table 1). Comparison of the *DAR*s for AF and all dextran polymers revealed an unexpected finding (Fig. 6): the anisotropy was increasing from the smallest AF molecule through dex75 but it reached a plateau for the three largest dextran polymers. Statistical ANOVA analysis confirmed a statistically significant difference among the molecular groups ($p < 0.001$), justifying a pairwise comparison. A post hoc Tukey test showed that the values of *DAR* obtained for the three largest (plateau-forming) molecules, average *DAR* = 1.78, are significantly higher than the *DAR* of AF and dex3 ($p < 0.05$).

TABLE 1 Diffusion of AF and dextran polymers measured with IOI method

		Agarose gel			Molecular layer of isolated turtle cerebellum				
Molecule	MW	D (10^{-7} cm^2 s^{-1})	d_H (nm)	d_G (nm)	D^*_{major} (10^{-7} cm^2 s^{-1})	λ_{major}	D^*_{minor} (10^{-7} cm^2 s^{-1})	λ_{minor}	*DAR*
AF	547	43.69 ± 2.71 (28)	1.1	1.7	21.23 ± 1.15 (12)	1.44 ± 0.03	14.36 ± 1.09	1.75 ± 0.06	1.48 ± 0.07
dex3	3000	23.25 ± 1.46 (20)	2.1	3.2	8.95 ± 1.31 (32)	1.63 ± 0.12	5.65 ± 0.83	2.05 ± 0.15	1.58 ± 0.13
dex75	75,000	4.16 ± 0.16 (11)	11.8	17.7	1.24 ± 0.11 (10)	1.84 ± 0.08	0.70 ± 0.09	2.45 ± 0.16	1.77 ± 0.17
dex282	282,000	2.34 ± 0.13 (10)	21.0	31.5	0.49 ± 0.09 (13)	2.21 ± 0.19	0.28 ± 0.06	2.97 ± 0.31	1.81 ± 0.20
dex525	525,000	1.54 ± 0.09 (11)	31.8	47.9	0.23 ± 0.05 (9)	2.63 ± 0.32	0.13 ± 0.04	3.49 ± 0.55	1.76 ± 0.18

Data are expressed as mean ± SD. Total number of records is shown in parentheses. Diffusion coefficients shown here were obtained at or corrected to 25°C (see Materials and Methods for details). $d_H = kT/(3\pi\eta D)$, where d_H is hydrodynamic diameter, k is Boltzmann's constant, T is absolute temperature, and η is the viscosity of water. $d_G = d_H/0.665$, where d_G is gyration diameter. $\lambda = (D/D^*)^{1/2}$. $DAR = D^*_{major}/D^*_{minor}$.

DISCUSSION

The IOI method was originally developed to measure the extracellular diffusion of fluorescent and fluorophore-labeled molecules in isotropic brain tissue (8,9). Visualization of the diffusion cloud together with rigorous quantification make the IOI method a potentially powerful tool to study diffusion in anisotropic brain regions. Here we extended the theory of IOI for anisotropic media, implemented two approaches to estimate the *DAR*, and measured the diffusion of AF and a series of fluorophore-labeled flexible random-coil polymers in the anisotropic ML of isolated turtle cerebellum. For all molecules tested, images of diffusing molecules acquired an elliptical shape with major and minor axes oriented along and across, respectively, the unmyelinated parallel fibers in the ML. The diffusion along both axes became more hindered as the size of the molecules increased with the *DAR* also increasing. Surprisingly, however, the *DAR* reached a plateau for dex75, dex282, and dex525.

Methods to measure anisotropic extracellular diffusion

Apart from DTI and RTI, two fluorescence-recovery-after-photobleaching-based optical methods, elliptical surface photobleaching (ESP; (4)) and fluorescence imaging of continuous point photobleaching (FICPP; (21)), have recently been applied to measure anisotropic diffusion in tissue.

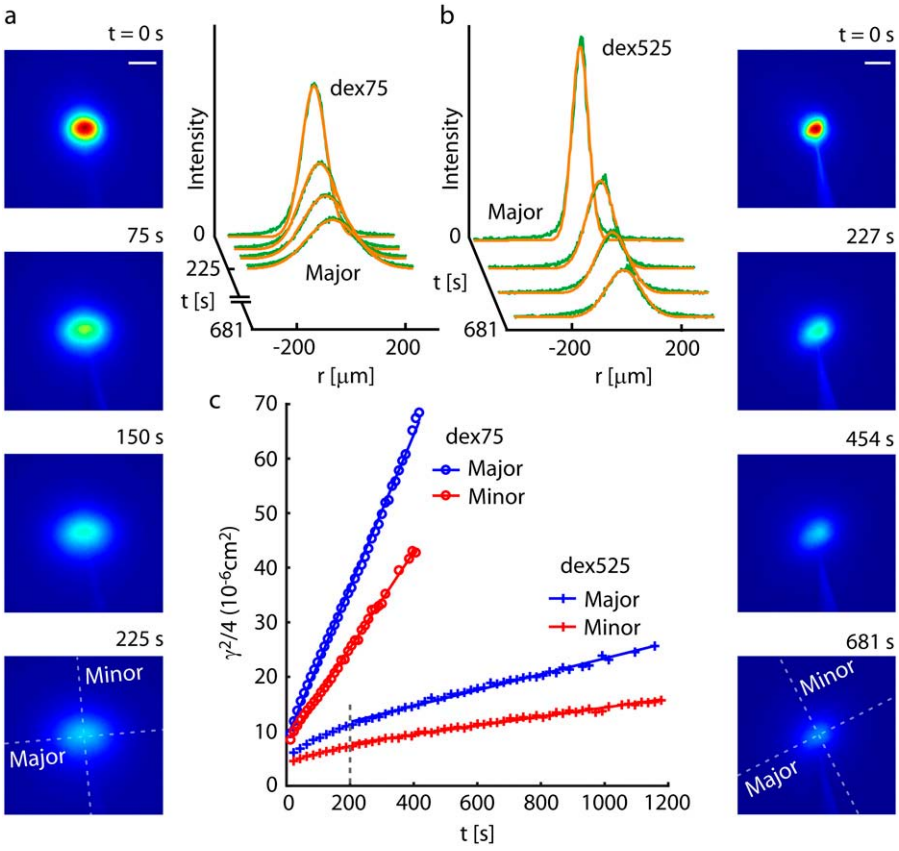

FIGURE 5 Anisotropic diffusion of dextran polymers in ML of isolated turtle cerebellum. Images and intensity profiles (*green*) superimposed with theoretical curves (*orange*) for dex75 (*a*) and dex525 (*b*) are shown (scale bar 100 μm). (*c*) The $\gamma^2/4$ versus time curves (*circles*, dex75; *crosses*, dex525; *lines*, linear regression) yielded D^*_{major} and D^*_{minor} values 1.39 × 10^{-7} cm^2 s^{-1} and 0.88 × 10^{-7} cm^2 s^{-1}, respectively, for dex75 at 25.5°C, and 0.14 × 10^{-7} cm^2 s^{-1} and 0.08 × 10^{-7} cm^2 s^{-1}, respectively, for dex525 at 24°C. Linear regression lines for dex75 are steeper indicating higher values of D^*_{major} and D^*_{minor}. For dex525, data obtained for $t < 200$ s (*dashed vertical line*) show nonlinearity and were excluded from the analysis.

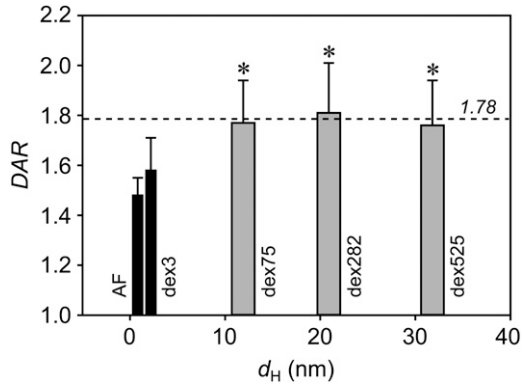

FIGURE 6 Summary of *DAR* values measured with AF and dextran polymers. The *DAR* for a group of dex75, dex282, and dex525 is significantly larger (*asterisks*) than for AF and dex3 (see text for details). Dotted line shows the plateau at $DAR = 1.78$.

The ESP was the first method to quantify macromolecular diffusion in the ECS of an anisotropic brain area, specifically the white matter of mouse spinal cord in vivo (4), while the FICPP was applied to collagenous connective tissue (21). In these methods, fluorophore-labeled dextran polymers are delivered to the tissue by bath application. In the ESP method, an elliptical spot having its major axis aligned either along or across the fibers was bleached and the fluorescence recovery was measured. In the FICPP method, a spot was continuously bleached as the images were acquired. The ESP and FICPP methods can provide data on anisotropic diffusion of a wide range of fluorescent molecules in the tissue but they have some notable limitations.

First, both methods require a homogenous distribution of fluorescent molecules, confined to the ECS. During the incubation period, molecules might enter cells, thus adding an intracellular component to the signal. Additionally, if physiologically relevant molecules, such as growth factors are employed, the prolonged exposure of the tissue to such molecules may alter the extracellular environment at the recording site. Second, bleaching with a laser light might bring about tissue damage. Third, the plane containing the fibers has to be correctly identified in both methods. The FICPP method then determines the major and minor axes from a two-dimensional image and quantifies the *DAR*; D^* is not obtained. For the ESP, the investigator also has to identify the orientation of fibers in the plane to align the elliptical photobleaching spot along and across the fibers. Inaccuracies in the alignment influence the *DAR* quantification, and consequently the *DAR*-based estimate of D^*. This may be the reason why a standard deviation equal to 80% of the *DAR* mean was reported by Papadopoulos et al. (4).

In the IOI method, no dye incubation is needed because the fluorescent molecules are released locally into the tissue. However, the injection must release very small volumes (in a subnanoliter range) to avoid tissue damage. Photodamage is not a concern in the IOI method as the tissue receives only brief exposures to a relatively weak light from a xenon lamp. Similarly to the ESP and FICPP, the plane where the fibers are localized needs to be correctly identified but, unlike either of the photobleaching methods, the IOI method can quantify both the *DAR* and the D^* from a single image sequence. One useful improvement of the IOI method, especially for the studies on anisotropy, would be the acquisition of a detailed z-stack of images to estimate the diffusion tensor regardless of the orientation of the preparation; this improvement would likely require the use of confocal or two-photon techniques (24) and might introduce problems with photobleaching.

Anisotropic diffusion of AF in brain ECS measured with IOI

The D^* values for the small AF molecule measured along the major and minor axes gave a *DAR* value of 1.48. This experimental *DAR* can be compared with model predictions based on the diffusion of point particles in an environment occupied by aligned elongated cells (25,26). When these cells are packed so as to leave a 30% volume fraction for the ECS, which matches the experimentally determined value of ECS volume fraction for the turtle ML (1), the simulated *DAR*s are in the range from 1.5 for a periodic arrangement of fiber elements five times longer than they are wide (estimated from Fig. 4 in (25)), to 1.7 for infinitely long fibers (based on Eq. 27a in (26)). The aligned parallel fibers may thus account for anisotropy in the ML. However, there are at least two caveats. First, the parallel fibers occupy <70% of the tissue volume, and second, the experiment indicates that $D^*_{\text{major}} < D$ whereas the models have $D^*_{\text{major}} \approx D$. The experimental D^*_{major} value likely reflects the imperfect alignment of fibers in turtle ML (27), leading to a lower *DAR*. Other factors present in the tissue but not incorporated in the model, such as numerous cellular processes misaligned with the parallel fibers, or interactions with the extracellular matrix and plasma membranes as proposed for the spinal cord tracts by Papadopoulos et al. (4), may also affect D^* but are less likely to contribute to anisotropy.

The DAR_{AF} measured in turtle ML is comparable to the anisotropy measurements with the RTI method in corpus callosum of P21-23 rats in vivo ((3), $\alpha = 0.26$, $DAR_{\text{TMA}} = 1.36$), and in the isolated spinal cord of P7-8 rats ((2), $\alpha = 0.27$, $DAR_{\text{TMA}} = 1.31$). Surprisingly, application of the RTI method in turtle ML (1), which contains less orderly fibers than the white matter tracts, obtained $DAR_{\text{TMA}} = 1.85$. This higher value arises from large tortuosity across the fibers ($\lambda_{y,\,\text{TMA}} = 1.95$ while $\lambda_{y,\,\text{AF}} = 1.75$); the tortuosity along the fibers was similar to our measurement ($\lambda_{x,\,\text{AF}} = \lambda_{x,\,\text{TMA}} = 1.44$).

Comparison of these results reiterates the question of the cause of anisotropy in brain regions containing fiber tracts. Theoretical and experimental results obtained with DTI have suggested that an orderly arrangement of axonal membranes is the primary cause of anisotropy while the degree of anisotropy can be modulated by myelination (12). However,

DTI works with a mixture of extracellular and intracellular signals. This may lead to much higher values of *DAR* because the diffusion of water inside the fibers is constrained by the membranes, thus significantly reducing the apparent diffusion coefficient across the fibers. Data obtained with all methods suggest that the geometry of fiber tracts does significantly contribute to the ECS anisotropy but the role of other factors needs further investigation.

Dependence of *DAR* on molecular size

We showed that in the anisotropic ML, D^*_{major} and D^*_{minor} decreased as the molecular weight increased. The dependence of D^* and λ on the size of the diffusing molecule was reported previously in isotropic brain regions ((8,28–31); but see (32)). To the best of our knowledge, this is the first study that quantifies the diffusion of a series of molecules spanning a 1000-fold difference in MW (547–525,000) in an anisotropic brain region. While D^* decreased monotonically as expected, the *DAR* showed a bimodal behavior: an increase for AF through dex75 followed by a plateau.

The initial increase in the *DAR* (from 1.48 to 1.77) qualitatively agrees with the prediction of a model examining the diffusion of hard spheres between parallel rods (33). Han and Herzfeld's model (33) predicts an increase in the *DAR* as the size of the sphere gets larger. Recent experiments in anisotropic collagenous tissues (21) support the general trend predicted by Han and Herzfeld's model, although the experimental results did not match the model quantitatively.

In contrast to the monotonic increase of the *DAR* with size for smaller molecules, we observed no *DAR* increase for dextran polymers larger than dex75. This result suggests that either the cerebellar ML environment or the diffusing dextran macromolecule behaves in a more complicated manner than expected.

The first possible explanation could lie with the structure of the diffusion environment. The parallel fibers are not the only geometrically ordered elements in the cerebellar ML. The vast and largely planar dendritic trees of Purkinje cells may represent additional obstacles in a direction perpendicular to the parallel fibers. Small molecules may get around these dendritic processes easily while larger molecules could be increasingly hindered by them. It is conceivable that the combined effect of the mutually perpendicular parallel fibers and dendritic trees could work against the expected increase of anisotropy with molecular size, thus creating the plateau shown in Fig. 5.

A second possibility based on the properties of the diffusion environment is that the parallel fibers to some degree dynamically adjust to accommodate passage of larger molecules. It has been documented that neuronal and glial processes are capable of dynamic behavior (34,35), even though the required degree of flexibility would be considerable given the large span of molecular diameters in our experiments.

Explanations based on the properties of brain diffusion environment, however, encounter difficulty reconciling the tortuosities obtained with dextran polymers with those reported for quantum dots of a similar hydrodynamic diameter. While λ_{major} and λ_{minor} for dex525 ($d_H = 31.8$ nm) were only 2.6 and 3.5, respectively, much larger $\lambda = 10.6$ was reported for quantum dots ($d_H = 35.4$ nm) in the rat neocortex in vivo (31). Even though these results were obtained in different species and brain regions, it seems likely that the properties of the diffusing molecules rather than the environment determine the diffusion behavior of larger dextrans.

We argue that the most likely explanation of the *DAR* plateau is that dextrans are flexible polymers (36, 37), free to change their shape when constrained by the environment. This flexibility arises from large conformational freedom of the α-1,6 linkage connecting the D-glucan units into a chain, which allows these polymers to diffuse through pores of a width smaller than the molecular hydrodynamic diameter (36). We propose that diameters of dex282 and dex525 approach the width of the channels in the ECS, compelling these flexible polymers to change conformation into a more elongated form to diffuse.

The importance of molecular shape for transport in the brain interstitium was previously demonstrated by Prokopová-Kubinová et al. (18), who showed that for linear polymers composed of poly[N-(2-hydroxypropyl) methacrylamide] with molecular weights up to 1,057,000 the tortuosities were surprisingly small, in the range of only 1.5–1.7 in the rat neocortex in vitro. We note, however, that direct comparison of the poly[N-(2-hydroxypropyl) methacrylamide] result with our data has to be undertaken with caution. In addition to working with a different species and a different brain region, Prokopová-Kubinová and co-workers acquired their image sequences over relatively short times ($\approx$200 s), even for the largest polymers. In our study, these early times were excluded from the analysis because of nonlinearity of the $\gamma^2/4$ versus time curve (see Results).

Scaling theory offers an explanation for diffusion behavior of dextran polymers

We sought support for our interpretation of the *DAR* plateau from scaling theory developed in polymer physics (38). Scaling theory separates the diffusion behavior of polymer chains in porous media into two regimes based on the relationship between the diameter of gyration ($d_G = d_H/0.665$; (39)) and the pore width (a), with a transition in the diffusion behavior at $d_G = a$. When $d_G < a$, the diffusive behavior of a polymer chain is described by the Zimm model ($D \propto \text{MW}^{-0.5}$; (40)). For $d_G > a$, reptation theory ($D \propto \text{MW}^{-2}$) is applicable (38). We applied scaling theory to test whether the diffusion behavior of the two largest dextran polymers was consistent with the reptation regime. A good correlation would support the possibility of a conformational change of larger dextrans

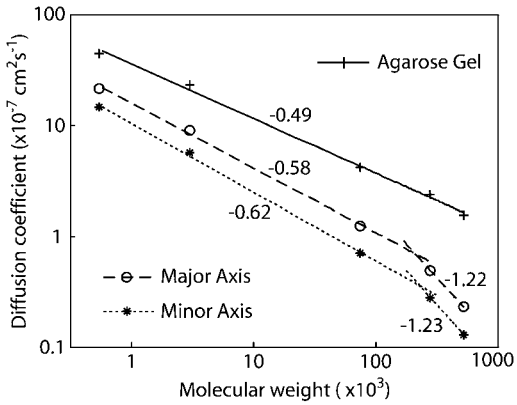

FIGURE 7 Application of scaling theory to the experimental data. Diffusion coefficients of AF and dextran polymers are plotted as a function of molecular weight in agarose gel (*solid line*) and the ML of isolated turtle cerebellum (*dashed line*, major axis; *dotted line*, minor axis). Scaling exponents are shown. In the agarose gel, scaling exponent obtained for all molecules agrees with Zimm's prediction. In the ML, diffusion of AF, dex3, and dex75 in the ML also is consistent with Zimm's prediction. In contrast, diffusion behavior of two largest dextran polymers (dex282 and dex525) is consistent with a reptation regime. The intersections of two different regimes estimate the average size of ECS at 31 nm (see text for details).

in brain ECS. Furthermore, the transition point would provide an estimate of the average width of the ECS in the ML.

The diffusion coefficients of AF and dextran polymers were plotted as a function of the molecular weight in Fig. 7, using a log-log scale. In agarose gel, the slope of the curve gave a scaling exponent of -0.49, which agrees well with the Zimm model (40) and other experimental observations (41,42). In the ML, the diffusion of dextran molecules fell into two different regimes. For AF and the two smaller dextrans (dex3 and dex75), the D^* of dependence on the MW gave a scaling exponent of –0.58 for the major axis and –0.62 for the minor axis. These exponents are in a reasonably good agreement with Zimm's prediction. By contrast, the two larger dextrans (dex282 and dex525) gave a scaling exponent of –1.22 for the major axis and -1.23 for the minor axis. Although theory predicts a scaling component of –2.0 for the reptation regime, we consider our data to be in quite good agreement, given that a scaling exponent of -1.55 was obtained with DNA chain molecules in a well-characterized artificial medium consisting of 2% agar gel (42).

As mentioned above, a equals d_G at the intersection of the two scaling regimes, permitting an estimate of the average width of the interstitial spaces in the ML of the isolated turtle cerebellum. The two regimes intersected approximately at MW 211,000 and MW 232,000 for the major and minor axes, respectively (Fig. 7). To obtain d_G for these molecules, we first used the correlation $D = 8.63 \times 10^{-5}\ \mathrm{MW}^{-0.48}$, applicable for dextrans at 25°C (43, 44) to calculate free diffusion coefficients. All our experimental data in agarose gel are in good agreement with this relation. The resulting D values (2.40×10^{-7} cm^2 s^{-1} and 2.29×10^{-7} cm^2 s^{-1} for MW 211,000 and MW 232,000, respectively) were used to calculate d_H with the Stokes-Einstein equation ($d_H = kT/(3\pi\eta D)$, where k is Boltzmann's constant, T is the absolute temperature, and η is the viscosity of water). Finally, d_G was calculated. The width of the interstitial gaps was thus estimated to be 30.7 nm and 32.2 nm for the major and minor axes, respectively, to give an average value of 31 nm.

An important but unexpected outcome of our study is the above estimate of the average ECS width in the living tissue. Because of their minute dimensions, the interstitial spaces are impossible to visualize in the living tissue and this parameter is therefore typically measured in fixed tissue with electron microscopy (EM). The value of 20–25 nm obtained in mice cerebellar ML prepared for EM by freeze substitution (45) is lower than our estimate of ~31 nm in the turtle. The lower value in mice likely reflects movement of water between extra- and intracellular compartments during processing of the tissue for EM (45). Although difference in ECS width between the two species cannot be excluded, it is less likely. Another estimate based on diffusion experiments with dextrans and quantum dots in rat neocortex was reported by Thorne and Nicholson (31), who employed the restricted diffusion theory (46,47) to put the ECS width in the range of 38–64 nm.

In conclusion, this study demonstrates the utility of diffusion analysis in unraveling some of the complexities of the ECS structure, quantifying the diffusion coefficients of molecules, and obtaining parameters of the brain microstructure, e.g., the width of interstitial gaps in living tissue. The results have significance for the transport of molecules and drugs in the ECS and for generation of models with realistic parameters to study neurotransmitter diffusion, particularly during ectopic release (48,49) and spillover (50), which have been shown to mediate extrasynaptic signaling between cells in the ML of cerebellum.

The research was supported by the National Institutes of Health's National Institute of Neurological Disorders and Stroke, grant No. NS047557 (to S.H.) and grant No. NS28642 (to C.N.)

REFERENCES

1. Rice, M. E., Y. C. Okada, and C. Nicholson. 1993. Anisotropic and heterogeneous diffusion in the turtle cerebellum: implications for volume transmission. *J. Neurophysiol.* 70:2035–2044.
2. Prokopová, Š., L. Vargová, and E. Syková. 1997. Heterogeneous and anisotropic diffusion in the developing rat spinal cord. *Neuroreport.* 8:3527–3532.
3. Voříšek, I., and E. Syková. 1997. Evolution of anisotropic diffusion in the developing rat corpus callosum. *J. Neurophysiol.* 78:912–919.
4. Papadopoulos, M. C., J. K. Kim, and A. S. Verkman. 2005. Extracellular space diffusion in central nervous system: anisotropic diffusion measured by elliptical surface photobleaching. *Biophys. J.* 89:3660–3668.
5. Bjelke, B., R. England, C. Nicholson, M. E. Rice, J. Lindberg, M. Zoli, L. F. Agnati, and K. Fuxe. 1995. Long distance pathways of diffusion for dextran along fiber bundles in brain. Relevance for volume transmission. *Neuroreport.* 6:1005–1009.
6. Verma, I. M., and N. Somia. 1997. Gene therapy: promises, problems and prospects. *Nature.* 389:239–242.

7. Jain, R. K. 1998. The next frontier of molecular medicine: delivery of therapeutics. *Nat. Med.* 4:655–657.
8. Nicholson, C., and L. Tao. 1993. Hindered diffusion of high molecular weight compounds in brain extracellular microenvironment measured with integrative optical imaging. *Biophys. J.* 65:2277–2290.
9. Tao, L., and C. Nicholson. 1995. The three-dimensional point spread functions of a microscope objective in image and object space. *J. Microsc. Oxford.* 178:267–271.
10. Moseley, M. E., Y. C. Cohen, J. Kucharczyk, H. S. Asgari, M. F. Wendland, J. Tsuruda, and D. Norman. 1990. Diffusion-weighted MR imaging of anisotropic water diffusion in cat central nervous system. *Radiology.* 176:439–445.
11. Basser, P. J. 1995. Inferring microstructural features and the physiological state of tissue from diffusion-weighted images. *NMR Biomed.* 8:333–344.
12. Beaulieu, C. 2002. The basis of anisotropic water diffusion in the nervous system—a technical review. *NMR Biomed.* 15:435–455.
13. Nicholson, C., and J. M. Phillips. 1981. Ion diffusion modified by volume fraction and tortuosity in the extracellular microenvironment of the rat cerebellum. *J. Physiol.* 321:225–257.
14. Hrabětová, S., and C. Nicholson. 2007. Biophysical properties of brain extracellular space explored with ion-selective microelectrodes, integrative optical imaging and related techniques. *In* Electrochemical Methods for Neuroscience. A. C. Michael and L. M. Borland, editors. CRC Press, Taylor Francis Group, Boca Raton, FL.
15. Larsell, O. 1967. The Comparative Anatomy and Histology of the Cerebellum from Myxinoids through Birds. J. Jansen, editor. University of Minnesota Press, Minneapolis, MN.
16. Nicholson, C. 2001. Diffusion and related transport mechanisms in brain tissue. *Rep. Prog. Phys.* 64:815–884.
17. Cragg, S. J., C. Nicholson, J. Kume-Kick, L. Tao, and M. E. Rice. 2001. Dopamine-mediated volume transmission in midbrain is regulated by distinct extracellular geometry and uptake. *J. Neurophysiol.* 85:1761–1771.
18. Prokopová-Kubinová, Š., L. Vargová, L. Tao, K. Ulbrich, V. Šubr, E. Syková, and C. Nicholson. 2001. Poly[N-(2-hydroxypropyl)methacrylamide] polymers diffuse in brain extracellular space with same tortuosity as small molecules. *Biophys. J.* 80:542–548.
19. Philippoff, W. 1963. Viscosity of liquids. *In* American Institute of Physics Handbook. D.W. Gray, editor. McGraw-Hill, New York.
20. Carslaw, H. S., and J. C. Jaeger. 1997. Conduction of Heat in Solids, 2nd Ed. Oxford University Press, Oxford, UK.
21. Leddy, H. A., M. A. Haider, and F. Guilak. 2006. Diffusional anisotropy in collagenous tissues: fluorescence imaging of continuous point photobleaching. *Biophys. J.* 91:311–316.
22. Nicholson, C. 1985. Diffusion from an injected volume of a substance in brain tissue with arbitrary volume fraction and tortuosity. *Brain Res.* 333:325–329.
23. Fitzgibbon, A., M. Pilu, and R. B. Fisher. 1999. Direct least square fitting of ellipses. *IEEE Trans. Pattern Anal. Mach. Intell.* 21:476–480.
24. Stroh, M., W. R. Zipfel, R. M. Williams, W. W. Webb, and W. M. Saltzman. 2003. Diffusion of nerve growth factor in rat striatum as determined by multiphoton microscopy. *Biophys. J.* 85:581–588.
25. El-Kareh, A. W., S. L. Braunstein, and T. W. Secomb. 1993. Effect of cell arrangement and interstitial volume fraction on the diffusivity of monoclonal antibodies in tissue. *Biophys. J.* 64:1638–1646.
26. Hrabe, J., S. Hrabětová, and K. Segeth. 2004. A model of effective diffusion and tortuosity in the extracellular space of the brain. *Biophys. J.* 87:1606–1617.
27. Tolbert, D. L., B. Conoyer, and M. Ariel. 2004. Quantitative analysis of granule cell axons and climbing fiber afferents in the turtle cerebellar cortex. *Anat. Embryol.* (*Berl.*). 209:49–58.
28. Tao, L., and C. Nicholson. 1996. Diffusion of albumins in rat cortical slices and relevance to volume transmission. *Neuroscience.* 75:839–847.
29. Hrabětová, S. 2005. Extracellular diffusion is fast and isotropic in the stratum radiatum of hippocampal CA1 region in rat brain slices. *Hippocampus.* 15:441–450.
30. Hrabětová, S., J. Hrabe, and C. Nicholson. 2003. Dead-space microdomains hinder extracellular diffusion in rat neocortex during ischemia. *J. Neurosci.* 23:8351–8359.
31. Thorne, R. G., and C. Nicholson. 2006. In vivo diffusion analysis with quantum dots and dextrans predicts the width of brain extracellular space. *Proc. Natl. Acad. Sci. USA.* 103:5567–5572.
32. Binder, D. K., M. C. Papadopoulos, P. M. Haggie, and A. S. Verkman. 2004. In vivo measurement of brain extracellular space diffusion by cortical surface photobleaching. *J. Neurosci.* 24:8049–8056.
33. Han, J., and J. Herzfeld. 1993. Macromolecular diffusion in crowded solutions. *Biophys. J.* 65:1155–1161.
34. Bonhoeffer, T., and R. Yuste. 2002. Spine motility: phenomenology, mechanism, and function. *Neuron.* 35:1019–1027.
35. Hirrlinger, J., S. Hülsmann, and F. Kirchhoff. 2004. Astroglia processes show spontaneous motility at active synaptic terminals *in situ*. *Eur. J. Neurosci.* 20:2235–2239.
36. Bohrer, M. P., G. D. Patterson, and P. J. Carroll. 1984. Hindered diffusion of dextran and ficoll in microporous membranes. *Macromolecules.* 17:1170–1173.
37. Venturoli, D., and B. Rippe. 2005. Ficoll and dextran vs. globular proteins as probes for testing glomerular permselectivity: effects of molecular size, shape, charge, and deformability. *Am. J. Physiol. Renal Physiol.* 288:605–613.
38. de Gennes, P. G. 1979. Scaling Concepts in Polymer Physics. Cornell University Press, Ithaca, NY.
39. Tanford, C. 1961. Physical Chemistry of Macromolecules. J. Wiley & Sons. New York.
40. Doi, M., and S. F. Edwards. 1986. The Theory of Polymer Dynamics. Clarendon Press, Oxford University Press, Oxford and New York.
41. Smith, D. E., T. T. Perkins, and S. Chu. 1996. Dynamical scaling of DNA diffusion coefficients. *Macromolecules.* 29:1372–1373.
42. Pluen, A., P. A. Metti, R. K. Jain, and D. A. Berk. 1999. Diffusion of macromolecules in agarose gels: comparison of linear and globular configurations. *Biophys. J.* 77:542–552.
43. Granath, K. A., and B. E. Kvist. 1967. Molecular weight distribution analysis by gel chromatography on Sephadex. *J. Chromatogr. A.* 28: 69–81.
44. Nugent, L. J., and R. K. Jain. 1984. Extravascular diffusion in normal and neoplastic tissues. *Cancer Res.* 44:238–244.
45. Van Harreveld, A., J. Crowell, and S. K. Malhotra. 1965. A study of extracellular space in central nervous tissue by freeze-substitution. *J. Cell Biol.* 25:117–137.
46. Bungay, P. M., and H. Brenner. 1973. The motion of a closely-fitting sphere in a fluid-filled tube. *Intl. J. Multiphase Flow.* 1:25–56.
47. Deen, W. M. 1987. Hindered transport of large molecules in liquid-filled pores. *AIChE J.* 33:1409–1425.
48. Matsui, K., and C. E. Jahr. 2003. Ectopic release of synaptic vesicles. *Neuron.* 40:1173–1183.
49. Matsui, K., and C. E. Jahr. 2005. High-concentration rapid transients of glutamate mediate neural-glial communication via ectopic release. *J. Neurosci.* 25:7538–7547.
50. Szapiro, G., and B. Barbour. 2007. Multiple climbing fibers signal to molecular layer interneurons exclusively via glutamate spillover. *Nat. Neurosci.* 10:735–742.